

See discussions, stats, and author profiles for this publication at: <https://www.researchgate.net/publication/333807794>

An Aerodynamic Design Method of Propeller Airfoils with Geometric Compatibility as Constraints

Conference Paper · June 2019

DOI: 10.2514/6.2019-3493

CITATIONS

0

READS

360

4 authors:



Jianhua Xu

Northwestern Polytechnical University

19 PUBLICATIONS 29 CITATIONS

SEE PROFILE



Huijing Li

Northwestern Polytechnical University

1 PUBLICATION 0 CITATIONS

SEE PROFILE



Wenping Song

Northwestern Polytechnical University

108 PUBLICATIONS 454 CITATIONS

SEE PROFILE



Zhong-Hua Han

Northwestern Polytechnical University

112 PUBLICATIONS 1,384 CITATIONS

SEE PROFILE

Some of the authors of this publication are also working on these related projects:



Efficient Surrogate-based Optimization for High-Dimensional Aerodynamic Design [View project](#)



Design Optimization of Transonic Natural-Laminar-Flow Wing [View project](#)



An Aerodynamic Design Method of Propeller Airfoils with Geometric Compatibility as Constraints

Jian-Hua XU¹, Hui-Jing LI², Wen-Ping SONG^{3,*}, Zhong-Hua HAN⁴

National Key Laboratory of Science and Technology on Aerodynamic Design and Research, Northwestern Polytechnical University, Xi'an, 710072, China

The Mach number and Reynolds number vary widely from root to tip for a propeller blade, resulting complex flow at low-speed, subsonic and even transonic. Low-speed airfoils are used for inboard and high-speed airfoils are used for outboard, leading to a great challenge to ensure the aerodynamic compatibility and geometric compatibility of the airfoils under different design conditions. In this paper, some constraints, such as the locations of maximum thickness, coordinates of airfoils with adjacent thickness, and second-order derivative distribution of airfoil shape, are applied in the design optimization of propeller airfoil family, to achieve good geometric compatibility among airfoils. Reynolds-average Navier-Stokes (RANS) solver coupled with $\gamma - \overline{\text{Re}}_\theta$ transition model and the efficient optimizer “SurroOpt” are used to perform the optimization. The results show that the optimized airfoils with second-order derivative as constraints behave the best geometric compatibility, and the lift-to-drag ratio at the design condition is also improved significantly, which demonstrates that the proposed method is effective in the design of airfoil family for propeller.

Nomenclature

Ma	=	Mach number of the flow
Re	=	Reynolds number of the flow
α	=	angle of attack
c_l	=	lift coefficient
c_d	=	drag coefficient
c_{df}	=	friction drag coefficient
c_m	=	moment coefficient
$c_{l,cst}$	=	lift count
$c_{d,cst}$	=	drag count

I. Introduction

PROPELLERS are widely used in aeronautics, such as transport and high speed helicopter, which still have broad application in modern advanced aircraft. The performance of propeller airfoil plays a crucial role in improving propeller efficiency and characteristic under wide operating conditions. The airfoil family for propeller consists of a series of airfoils and the geometric compatibility as well as aerodynamic compatibility are important design constraints. The angle of attack at radial section can vary from 0° to angle of stall, and Mach number vary from 0.2

¹ Research Associate, School of Aeronautics, P. O. Box 754, Northwestern Polytechnical University, Youyi West Road, No. 127, xujh@nwpu.edu.cn.

² Graduate Student, School of Aeronautics, P. O. Box 754, Northwestern Polytechnical University, Youyi West Road, No. 127, huijing9612@qq.com.

³ Professor, School of Aeronautics, P. O. Box 754, Northwestern Polytechnical University, Youyi West Road, No. 127, wpsong@nwpu.edu.cn.

⁴ Professor, School of Aeronautics, P. O. Box 754, Northwestern Polytechnical University, Youyi West Road, No. 127, hanzh@nwpu.edu.cn.

to 0.9, and the blade geometric twist is large. Therefore, design of propeller airfoil considering geometric and aerodynamic compatibility is still a challenging problem.

The study and development of propeller have been in progress since 20 centuries. A series of dedicated airfoils for propeller were gradually developed. Currently, RAF series, ARA-D series, Clark series and NACA16 series are the most common airfoils for propellers^[1]. There are two methods for aerodynamic shape design of airfoil. The first one is numerical optimization method^{[2][3]}. In 1984, Frank Taverna^[4] described an aerodynamic design of an airfoil family shapes suitable for the blade of general aviation propeller with constraints of upper surface concavity, gradual lower surface contour, leading edge radius and trailing edge thickness. The other is inverse design method^{[5][6]} based on the velocity or pressure distribution along the surface defined by designer. The keystone and difficulty of the inverse method is that it requires designers' rich design experience. An inverse airfoil design was applied in propeller airfoil design by Jeffrey K. Jepson^[7] in 2005, which incorporated the propeller-powered airplanes' performance. Besides, the effect of second-order derivative and curvature of airfoil on aerodynamic performance of airfoil were also investigated by Shen X and D. Greenblatt^{[8][9]}.

Since the design of airfoil family for propeller needs pay attention to geometric compatibility among airfoils, this article proposes a new method to design an airfoil family for a propeller. Constraints including the locations of maximum thickness, coordinates of airfoils with adjacent thickness, and second-order derivative distribution of airfoil shape, are applied in the process of design optimization. Hence, this method not only improves the aerodynamic performance of single airfoil, but also ensures the geometric compatibility of airfoils with different thickness.

II. Flow Solver and Optimizer

A. Flow Solver and Grid Convergence Study

Currently, RANS solver has been widely used in aerodynamic analysis and design of airfoil. This article uses the in-house RANS solver--PMNS2D. Based on cell centered finite volume method, this solver is a numerical simulation program of two-dimensional flow. The spatial discretization scheme is Jameson's central scheme. The time marching method is implicit Lower-Upper Symmetric Gauss-Seidel^[10]. The turbulence model is two-equation SST $k-\omega$ model. $\gamma-\overline{Re}_\theta$ model is used for transition prediction, which is based on empiric formulas and local variables of flow field, presented by Menter and Langtry^[11].

Two test cases are presented for validation of the RANS solver: Figure 1 shows that the computed pressure distribution of RAE2822 airfoil agree well with the experimental data^[12] at the condition of $Ma = 0.734, Re = 6.5 \times 10^6, \alpha = 2.86^\circ$; Figure 2 demonstrates that the computed pressure distribution of S809 airfoil are in good agreement with the experimental data^[13] at the condition of $Ma = 0.1, Re = 2 \times 10^6, \alpha = 0^\circ$.

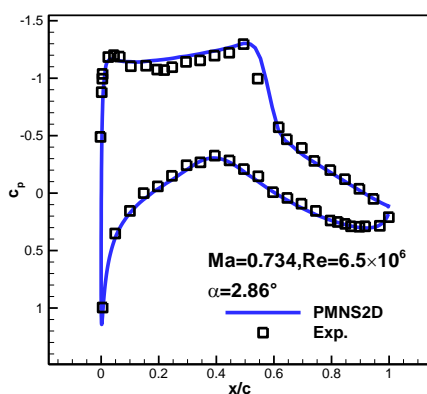


Figure 1. Comparison of the pressure distributions between computed results and experimental data of RAE2822

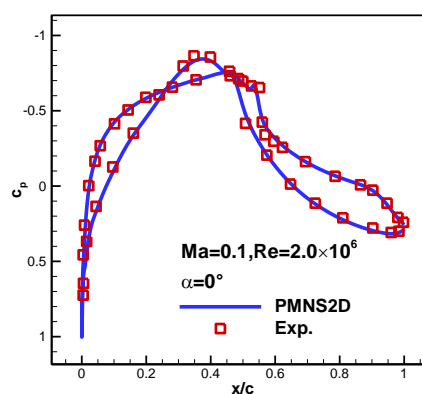


Figure 2. Comparison of the pressure distributions between computed results and experimental data of S809

In order to balance the efficiency of optimization and the reliability of results, grid convergence is studied first. Eight levels of C-type structure grids, named L1~L8, are used and the simulation results are shown in Table 1. From L1 to L8, the number of grid cells is increased sequentially. It shows that the difference of aerodynamic coefficients between L7 and L8 satisfies the requirement of convergence, $\Delta c_{l,cts} < 1$ and $\Delta c_{d,cts} < 1$. Thus, we use L7 to implement the following optimization works.

Table 1 Aerodynamic performance of the baseline airfoil for different grids of varying resolution
($Ma = 0.64, Re = 3.8 \times 10^6, \alpha = 1.5^\circ$) (1 lift count=0.001, 1 drag count=0.0001)

Grid size	$c_{l,cts}$	$\Delta c_{l,cts}$	$c_{d,cts}$	$\Delta c_{d,cts}$
L1(132×44)	984.082	14.75	118.50	21.71
L2(176×60)	998.832	5.844	95.79	2.59
L3(260×84)	1004.676	5.75	93.20	3.33
L4(352×116)	1010.426	5.672	89.87	1.52
L5(420×140)	1016.098	2.354	88.35	1.06
L6(500×160)	1018.452	2.247	87.29	0.34
L7(604×192)	1020.699	0.498	86.95	0.34
L8(704×224)	1021.197	-	86.61	-

B. The optimizer for Airfoil Design

The existing CFD-based aerodynamic optimization design methods can be classified into three categories: gradient-based optimization algorithms; heuristic optimization algorithms such as genetic algorithms, and surrogate-based optimization algorithms. The gradient optimization algorithm has the outstanding advantages of fast convergence and high efficiency, which is the dominant method currently, but it has a poor global search ability. The heuristic optimization algorithm such as genetic algorithm is a global optimization method, but it is very computational intensive and the efficiency is low. Surrogate-based optimization method, which has been classified as a third-class optimization algorithm in recent years^[16], has the advantages of both high efficiency and globality, it has been proved well suited for the problems where high-fidelity and expensive simulation are needed for the objective evaluation. The high-fidelity RANS simulations are used in this paper for the objective evaluation of propeller airfoil optimization, so we use the surrogate-based in-house optimizer SurroOpt^[16], the flow chart of the optimizer is shown in Figure 3. The user defined interface shown in Figure 4 is established in order to automate the processes of parameterization, grid generation, flow simulation, etc. CST (Class function/Shape function transformation) that is presented by Kulfan^{[17][18]} from Boeing Commercial Airplanes, is used for airfoil parameterization.

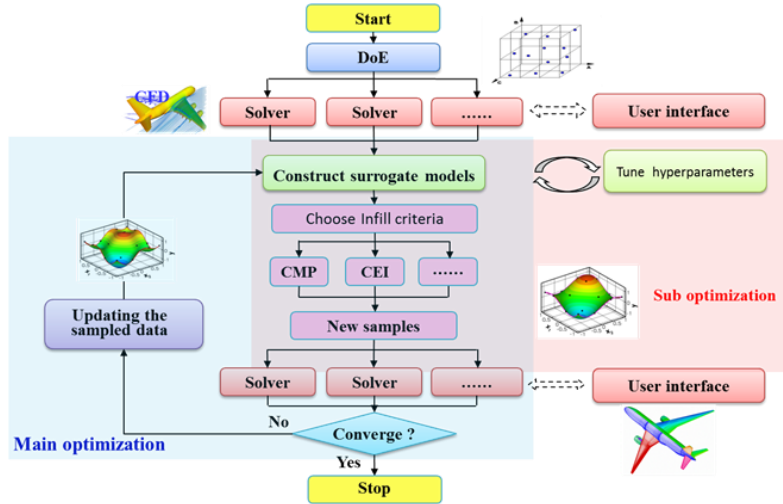


Figure 3. Flow chart of “SurroOpt”^[16]

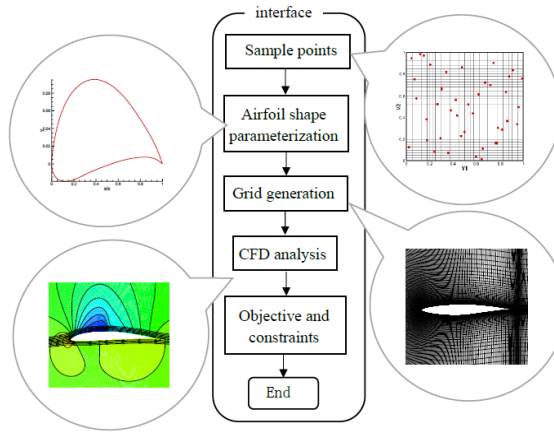


Figure 4. Flow chart of “interface”

C. Aerodynamic Design with Airfoil Geometric Compatibility as Constraints

The geometric compatibility in present work includes the locations of maximum thickness, y coordinates of airfoils at adjacent sections of propeller, and second-order derivative distribution of airfoil shape. Since the SurroOpt has a superior ability of handling constraints, these geometric compatibility constraints are enforced in the optimization process as follows:

(1) **Constraint 1: locations of maximum thickness.**

This constraint ensures the designed airfoils have almost the same location of maximum thickness, described as:

$$|x_{\max thk} - x_{\max thk,0}| \leq 0.01$$

where, $x_{\max thk}$ is the location of maximum thickness of design airfoil, and $x_{\max thk,0}$ is the location of maximum thickness specified by the designer.

(2) **Constraint 2: y coordinates of airfoils with adjacent thickness.**

This constraint ensure airfoil with larger thickness (thicker) can fully surround the airfoil with smaller thickness (thinner), described as:

$$\min(y_{upper,thicker} - y_{upper,thinner}) \geq 0, \quad x \in (0,1)$$

$$\min(y_{lower,thinner} - y_{lower,thicker}) \geq 0, \quad x \in (0,1)$$

where, the subscript “upper” and “lower” means the upper and lower surface of airfoil, respectively.

(3) Constraint 3: second-order derivative distribution

In this paper, the constraint of second-order derivative distribution is proposed to improve the geometric compatibility. For upper surface, the second-order derivative of thicker airfoil is always lower than that of thinner airfoil; for lower surface, the second-order derivative of thicker airfoil is always higher than that of thinner airfoil. The mathematical model is described as follows:

$$\begin{aligned} \min(y''_{upper, thinner} - y''_{upper, thicker}) &\geq 0, \quad x \in (0, 1) \\ \min(y''_{lower, thicker} - y''_{lower, thinner}) &\geq 0, \quad x \in (0, 1) \end{aligned}$$

where, y'' means the second-order derivative.

III. Aerodynamic Design of Propeller Airfoils

A. Optimization Design without Geometric Compatibility as Constraints

In this part, the optimization design of airfoils with relative thicknesses of 12%, 14%, 16% and 20% are carried out, with commonly used aerodynamic optimization method.

A.1 Design of 12% thick airfoil

This section proposes the design of 12% thick airfoil, with the Mach number of 0.64, the Reynolds number of 3.8×10^6 , and the design lift coefficient is fixed to 1.1. The baseline airfoil PLRMS12 is designed for low Reynolds number propeller by our research group.

The mathematical model for aerodynamic optimization is described as follows:

$$\begin{aligned} \text{objective} \quad & \min c_d \\ \text{s.t.} \quad & 0.15 - |c_m| \geq 0 \\ & \text{thk} - 0.12 \geq 0 \end{aligned} \quad (1)$$

where, “thk” means the thickness of airfoil.

The comparison of shapes and pressure distribution between baseline and optimized airfoil are shown in Figure 5 and Figure 6. The aerodynamic force coefficients of baseline and optimized airfoil at the design condition are listed in Table 2. Compared to baseline airfoil, the drag coefficient is reduced by 30.2%, although the friction drag increase 1%. This shows that the shock wave drag is greatly reduced. Also, the pressure contours in Figure 7 demonstrates that the shock wave strength of the optimized airfoil is obviously weaker than that of the baseline airfoil. Therefore, the lift-to-drag ratio has a significant increment.

The performance curves of baseline and optimized airfoil are shown in Figure 8 to Figure 11. The symbol “OPT” means the optimized airfoil. The maximum lift coefficient of the optimized airfoil is higher than that of the baseline airfoil, with almost the same aerodynamic performance after stall. The drag coefficients under almost all lift coefficients are reduced, especially near the design lift coefficient, and the lift-to-drag ratio is significantly improved. Meanwhile, the moment characteristics have also been improved.

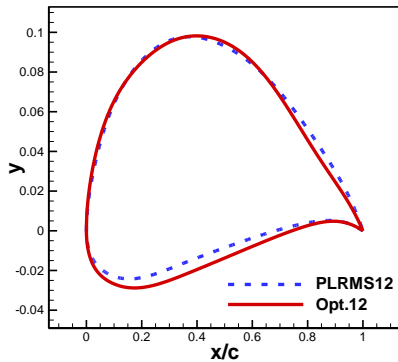


Figure 5. Comparison of shapes between baseline and optimized airfoils with 12% thickness-chord ratio

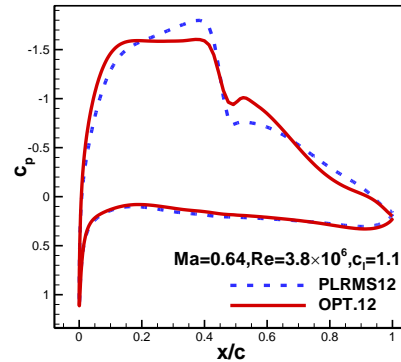


Figure 6. Comparison of pressure distributions between baseline and optimized airfoils with 12% thickness-chord ratio

Table 2 Comparison of aerodynamic force coefficients between baseline and optimized airfoils
($Ma = 0.64, Re = 3.8 \times 10^6, c_l = 1.1$)

	c_l	c_d	c_{dp}	c_{df}	c_m	L/D
Baseline airfoil	1.1	0.012898	0.008696	0.004202	-0.157484	85.28
Optimized airfoil	1.1	0.009004	0.004758	0.004246	-0.149649	122.17
Δ	/	-0.003894	-0.00394	+0.000044	+0.007835	+36.89
$\Delta(\%)$	/	-30.19	-45.31	+1.05	/	+43.26

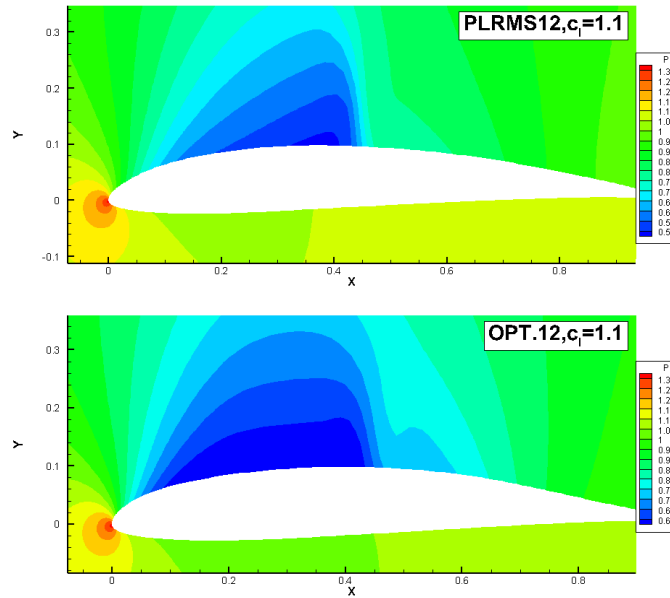


Figure 7. The contour of pressure distribution of baseline airfoil (PLRMS12) and optimized airfoil (OPT.12). The shock wave strength of optimized airfoil is weaker than baseline airfoil, which contributes a reduction of shock wave drag.

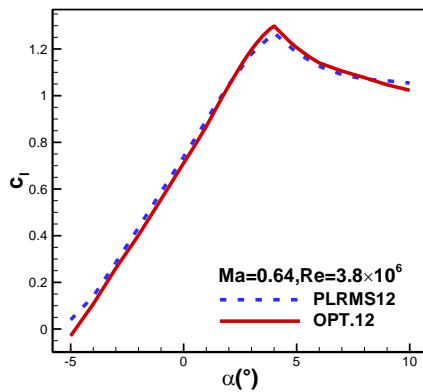


Figure 8. Comparison of the lift coefficients between baseline and optimized airfoils (12% c)

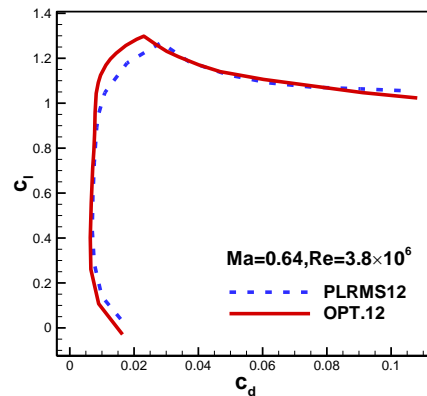


Figure 9. Comparison of the polar curves between baseline and optimized airfoils (12% c)

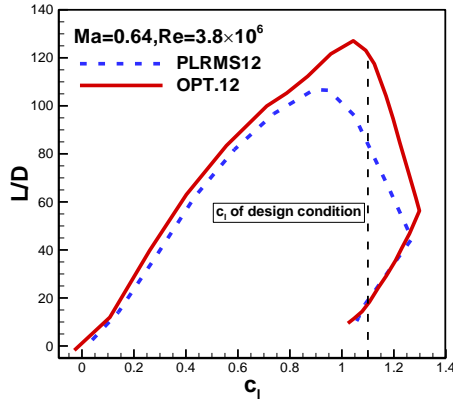


Figure 10. Comparison of the lift-drag ratio between baseline and optimized airfoils (12%*c*)

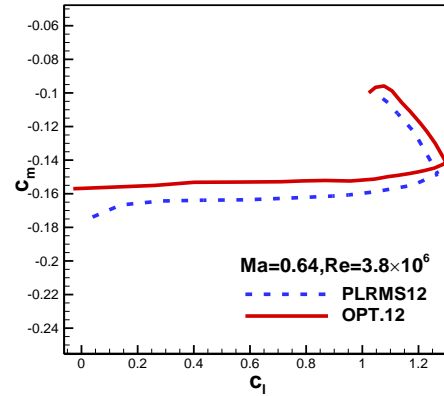


Figure 11. Comparison of the moment coefficients between baseline and optimized airfoils (12%*c*)

A.2 Design of 14%*c* thick airfoil

This section is the optimization of airfoil with the relative thickness of 14%, and the Mach number is 0.53, the Reynolds number of 3.0×10^6 , the design lift coefficient is fixed to 1.1.

The mathematical model for aerodynamic optimization is described as follows:

$$\begin{aligned} \text{objective} \quad & \min c_d \\ \text{s.t.} \quad & 0.15 - |c_m| \geq 0 \\ & \text{thk} - 0.14 \geq 0 \end{aligned} \quad (2)$$

The comparison of shapes and pressure distribution between baseline and optimized airfoil are shown in Figure 12 and Figure 13. The aerodynamic force coefficients of baseline and optimized airfoil at design condition are listed in Table 3. The drag coefficient is reduced by 16.35%, of which the friction drag account for 25%. Also, the pressure drag is reduced significantly. Thus, the lift-to-drag ratio has an increment by 19.5%.

The intermittency factor contour of baseline and optimized airfoils are shown in Figure 14 and Figure 15, respectively. The transition location of upper surface is postponed from 21%*c* of the baseline airfoil to 51%*c* of the optimized airfoil, and the transition location of lower surface is postponed from 37%*c* of the baseline airfoil to 48%*c* of the optimized airfoil. The laminar region of optimized airfoil is larger, resulting a reduction of friction drag.

The performance curves of baseline and optimized airfoil are shown in Figure 16 to Figure 19. The maximum lift coefficient of the optimized airfoil is higher than that of the baseline airfoil, with almost the same aerodynamic performance after stall. The drag coefficients under almost all lift coefficients are reduced, especially near the design lift coefficient, and the lift-to-drag ratio is significantly improved. Meanwhile, the moment characteristics have also been improved.

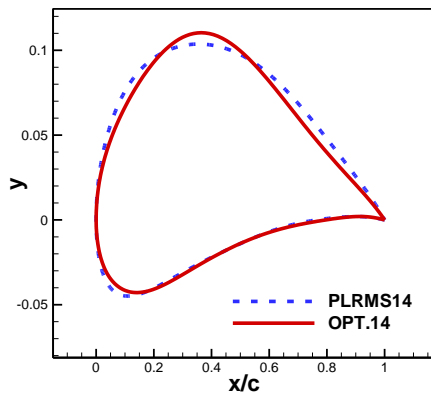


Figure 12. Comparison of the geometric shapes between baseline and optimized airfoils (14%*c*)

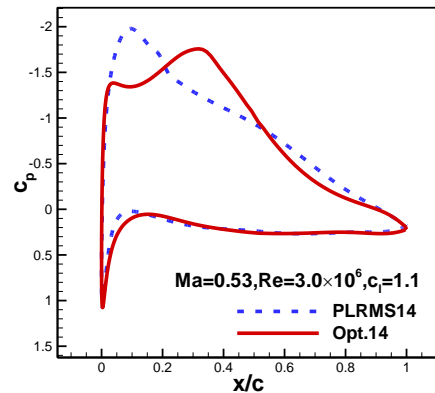


Figure 13. Comparison of the pressure distributions between baseline and optimized airfoils (14%*c*)

Table 3 Comparison of aerodynamic force coefficients between baseline and optimized airfoils
($Ma = 0.53, Re = 3.0 \times 10^6, c_l = 1.1$)

	c_l	c_d	c_{dp}	c_{df}	c_m	L/D
Baseline airfoil	1.1	0.010620	0.00566	0.004960	-0.118156	103.58
Optimized airfoil	1.1	0.008884	0.004362	0.004522	-0.118865	123.82
Δ	/	-0.001736	-0.0013	-0.000438	-0.000709	+20.24
$\Delta(\%)$	/	-16.35	-22.97	-8.83	/	+19.54

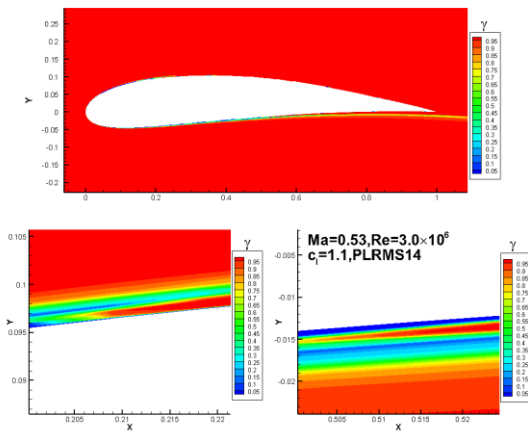


Figure 14. The contour of intermittency factor γ of baseline airfoil (14%c). The transition location of upper surface is about 21%c while the transition location of lower surface is about 51%c.

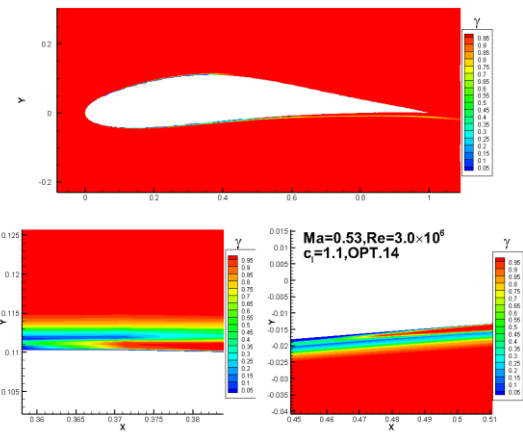


Figure 15. The contour of intermittency factor γ of optimized airfoil (14%c). The transition location of upper surface is about 37%c while the transition location of lower surface is about 48%c.

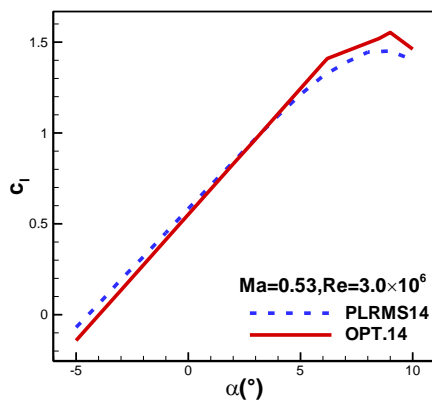


Figure 16. Comparison of the lift coefficients among baseline and optimized airfoils (14%c)

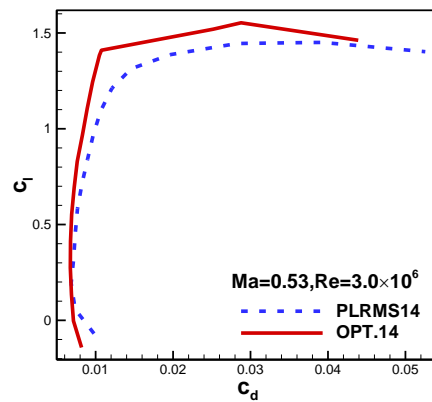


Figure 17. Comparison of the polar curves among baseline and optimized airfoils (14%c)

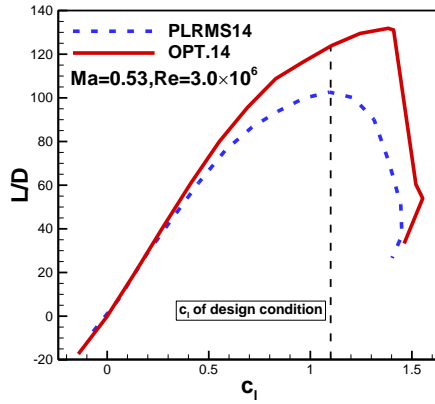


Figure 18. Comparison of the lift-drag ratio among baseline and optimized airfoils (14%c)

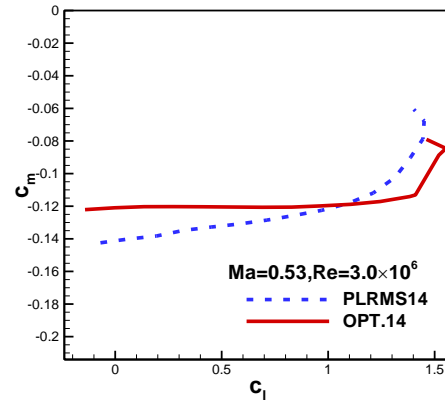


Figure 19. Comparison of the moment coefficients among baseline and optimized airfoils (14%c)

A.3 Design of 16%c thick airfoil

This section is the design of 16%c thick airfoil, with a Mach number of 0.44, a Reynolds number of 2.5×10^6 , and the design lift coefficient is fixed to 1.2.

The mathematical model for aerodynamic optimization is described as follows:

$$\begin{aligned} \text{objective} \quad & \min c_d \\ \text{s.t.} \quad & 0.15 - |c_m| \geq 0 \\ & \text{thk} - 0.16 \geq 0 \end{aligned} \quad (3)$$

The comparison of shapes and pressure distribution between baseline and optimized airfoil are shown in Figure 20 and Figure 21. The aerodynamic force coefficients of baseline and optimized airfoil at design condition are listed in Table 4. The drag coefficient is reduced by 15.98 %. Both the pressure drag and friction drag are reduced. Therefore, the lift-to-drag ratio has an increment by 19%.

The aerodynamic performance of baseline and optimized airfoil are shown in Figure 22 to Figure 25. The lift-to-drag ratio of optimized airfoil is higher under a wide range of lift coefficients.

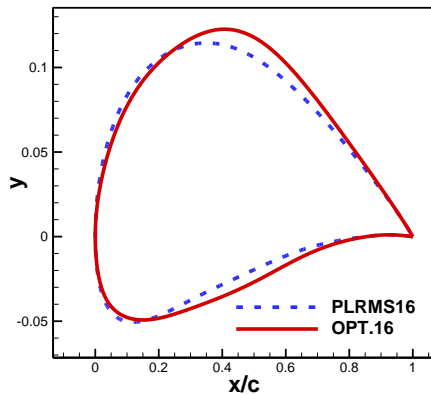


Figure 20. Comparison of the geometric shapes between baseline and optimized airfoils (16%c)

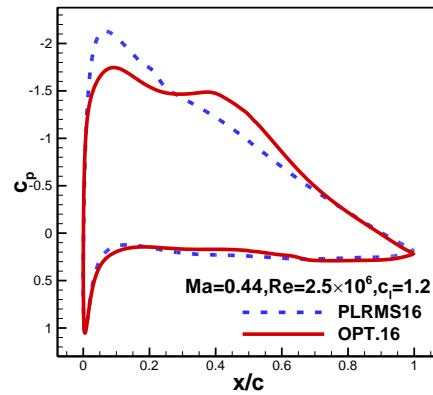


Figure 21. Comparison of the pressure distributions between baseline and optimized airfoils (16%c)

Table 4 Comparison of aerodynamic force coefficients between baseline and optimized airfoils
($Ma = 0.44, Re = 2.5 \times 10^6, c_l = 1.2$)

	c_l	c_d	c_{dp}	c_{df}	c_m	L/D
Baseline airfoil	1.2	0.011270	0.006624	0.004646	-0.111978	106.48
Optimized airfoil	1.2	0.009469	0.005334	0.004135	-0.135700	126.73
Δ	/	-0.001801	-0.00129	-0.000511	-0.023722	+20.25
$\Delta(\%)$	/	-15.98	-19.47	-11.00	/	+19.02

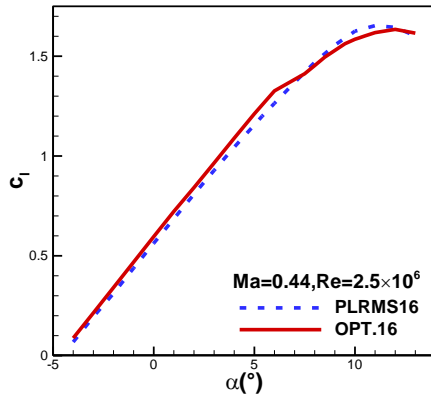


Figure 22. Comparison of the lift coefficients among baseline and optimized airfoils (16%c)

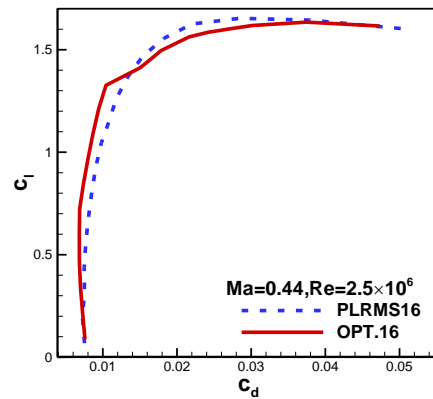


Figure 23. Comparison of the polar curves among baseline and optimized airfoils (16%c)

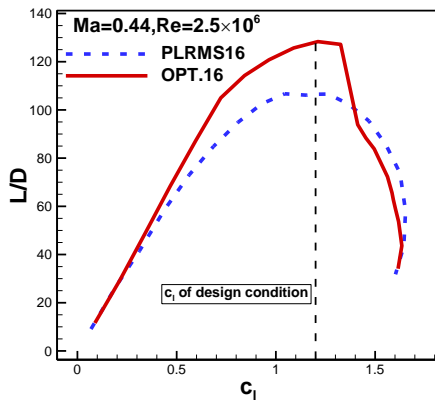


Figure 24. Comparison of the lift-drag ratio among baseline and optimized airfoils (16%c)

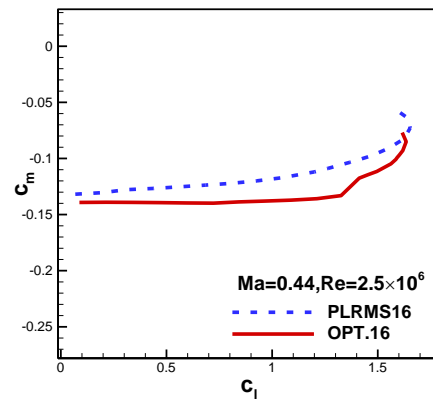


Figure 25. Comparison of the moment coefficients among baseline and optimized airfoils (16%c)

A.4 Design of 20%c thick airfoil

This section is the design of 20%c thick airfoil. The Mach number in this section is 0.4, with a Reynolds number of 2.0×10^6 , and the design lift coefficient is fixed to 1.2.

The mathematical model for aerodynamic optimization is described as follows:

$$\begin{aligned}
 &\text{objective} && \min && c_d \\
 &\text{s.t.} && 0.15 - |c_m| \geq 0 \\
 &&& \text{thk} - 0.20 \geq 0
 \end{aligned} \tag{4}$$

The comparison of the geometric shapes and the pressure distributions between baseline and optimized airfoils with 20% c thick are presented in Figure 26 and Figure 27. The aerodynamic force coefficients of baseline and optimized airfoil at design condition are listed in Table 5. The drag coefficient is reduced by 26.80%, of which the friction drag account for 12%. Also, the pressure drag is reduced significantly. Thus, the lift-to-drag ratio has an increment by 36.03%.

The performance curves of baseline and optimized airfoil are shown in Figure 28 to Figure 31. The maximum lift coefficient of the optimized airfoil is higher than that of the baseline airfoil, but the stall angle of attack is smaller. The drag coefficients are reduced under range of high lift coefficient, and the lift-to-drag ratio is significantly improved especially near the design lift coefficient. Meanwhile, the moment characteristics have also been improved significantly.

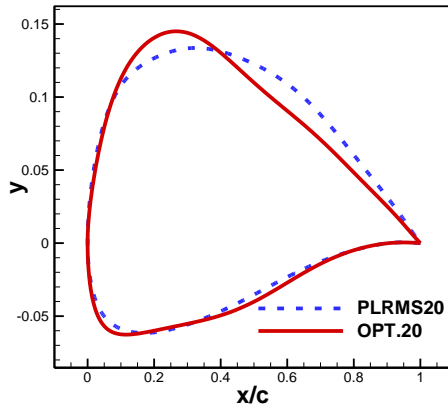


Figure 26. Comparison of the geometric shapes between baseline and optimized airfoils (20% c)

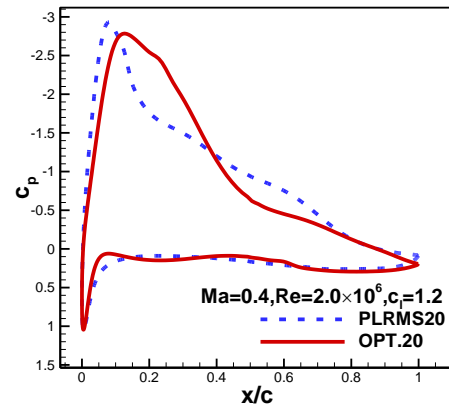


Figure 27. Comparison of the pressure distributions between baseline and optimized airfoils (20% c)

Table 5 Comparison of aerodynamic force coefficients between baseline and optimized airfoils
($Ma = 0.4, Re = 2.0 \times 10^6, c_l = 1.2$)

	c_l	c_d	c_{dp}	c_{df}	c_m	L/D
Baseline airfoil	1.2	0.016758	0.011426	0.005332	-0.095691	71.91
Optimized airfoil	1.2	0.012267	0.007478	0.004789	-0.083527	97.82
Δ	/	-0.004491	-0.003948	-0.000543	+0.012164	+25.91
$\Delta(\%)$	/	-26.80	-34.55	-10.18	/	+36.03

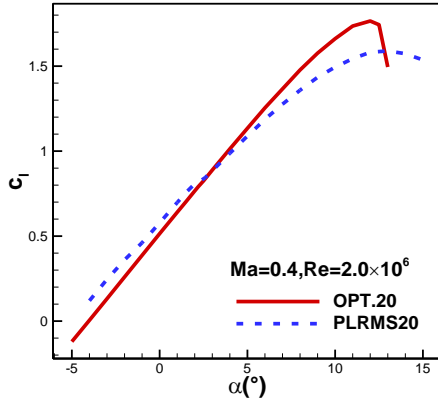


Figure 28. Comparison of the lift coefficients among baseline and optimized airfoils (20%c)

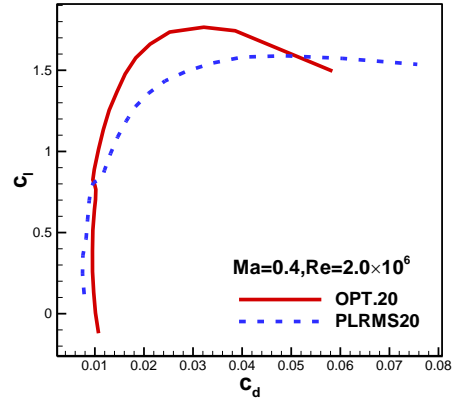


Figure 29. Comparison of the polar curves among baseline and optimized airfoils (20%c)

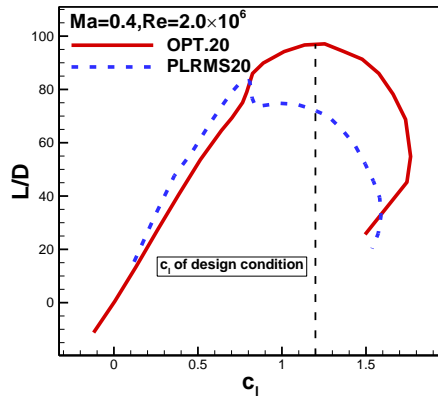


Figure 30. Comparison of the lift-drag ratio among baseline and optimized airfoils (20%c)

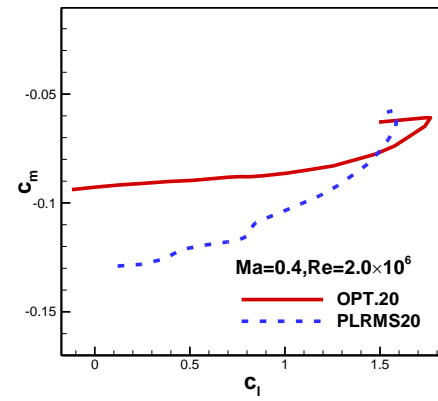


Figure 31. Comparison of the moment coefficients among baseline and optimized airfoils (20%c)

B. Geometric Compatibility Constraints: Location of Maximum Thickness and Coordinates of Airfoils with Adjacent Thickness

In this section, location of maximum thickness and coordinates of airfoils with adjacent thickness are applied as geometric compatibility constraints. Based on the above optimized 12% thick airfoil, 14%, 16% and 20% thickness of airfoils are optimized.

B.1 Design of 14% thick airfoil with geometric compatibility constraints

The design conditions are the same as section A.2. The mathematical model for aerodynamic optimization is described as follows:

$$\begin{aligned}
 &\text{objective} && \min c_d \\
 &\text{s.t.} && 0.15 - |c_m| \geq 0 \\
 &&& \text{thk} - 0.14 \geq 0 \\
 &&& |x_{\text{max thk}} - x_{\text{max thk}, 12\%c}| \leq 0.01 \\
 &&& \min(y_{\text{upper}} - y_{\text{upper}, 12\%c}) \geq 0 \\
 &&& \min(y_{\text{lower}, 12\%c} - y_{\text{lower}}) \geq 0
 \end{aligned} \tag{5}$$

where, the subscript "12%c" is the optimized airfoil with 12%c thickness.

The comparison of shapes and pressure distribution are shown in Figure 32 and Figure 33. The pressure distributions of the optimized airfoils with and without geometric compatibility constraints are similar, whereas their

shapes vary greatly. The optimized airfoil of 14% thickness without geometric compatibility constraints is partially inside the airfoil of 12% thickness, especially near the trailing edge on upper surface. While the optimized airfoil of 14% thickness with geometric compatibility constraints can fully surround the airfoil of 12% thickness.

The aerodynamic force coefficients of baseline and optimized airfoil with geometric compatibility at design condition are listed in Table 6. The drag coefficient is reduced by 18.55%, of which the friction drag accounts for 37%. Both the pressure drag and friction drag are reduced. Therefore, the lift-to-drag ratio has a significant increment by 23%.

The aerodynamic performance of baseline and optimized airfoil with and without geometric compatibility are shown in Figure 34 to Figure 37. The symbol “OPT” means optimized airfoil and the symbol “(y)” means the y coordinates of airfoils constraints. The maximum lift coefficient of the optimized airfoil with geometric compatibility is higher than that of the baseline airfoil and the optimized airfoil without geometric compatibility constraints. The drag coefficients under almost all lift coefficients are reduced, especially near the design lift coefficient, and the lift-to-drag ratio is significantly improved.

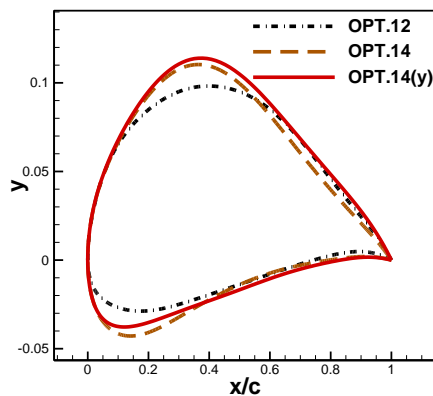


Figure 32. Comparison of the geometric shapes between adjacent and optimized airfoils with and without geometric compatibility (14% c)

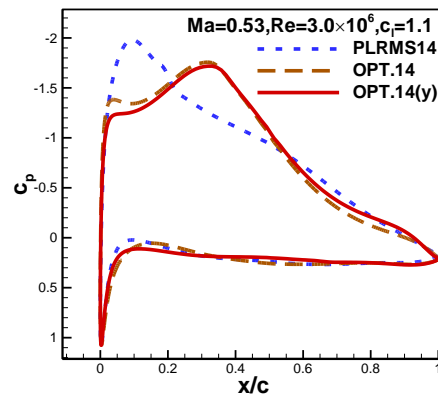


Figure 33. Comparison of the pressure distributions between baseline and optimized airfoils with and without geometric compatibility (14% c)

Table 6 Comparison of aerodynamic force coefficients between baseline and optimized airfoils
($Ma = 0.53, Re = 3.0 \times 10^6, c_l = 1.1$)

	c_l	c_d	c_{dp}	c_{df}	c_m	L/D
Baseline airfoil	1.1	0.010620	0.00566	0.004960	-0.118156	103.58
Optimized airfoil	1.1	0.008650	0.004414	0.004236	-0.133032	127.17
Δ	/	-0.001970	-0.00125	-0.000724	-0.014876	+23.59
$\Delta(\%)$	/	-18.55	-22.08	-14.60	/	+22.77

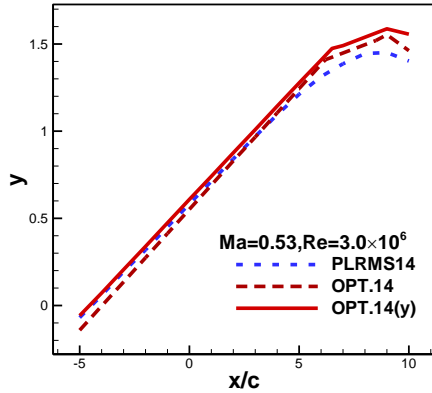


Figure 34. Comparison of the lift coefficients among baseline and optimized airfoils with and without geometric compatibility (14%c)

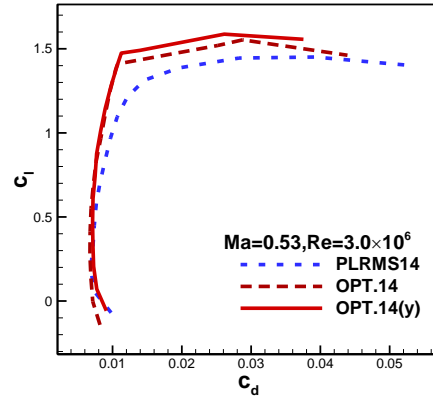


Figure 35. Comparison of the polar curves among baseline and optimized airfoils with and without geometric compatibility (14%c)

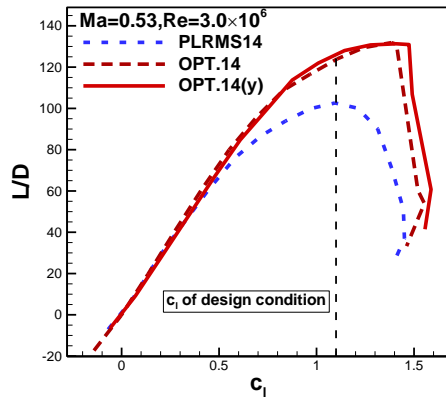


Figure 36. Comparison of the lift-drag ratio among baseline and optimized airfoils with and without geometric compatibility (14%c)

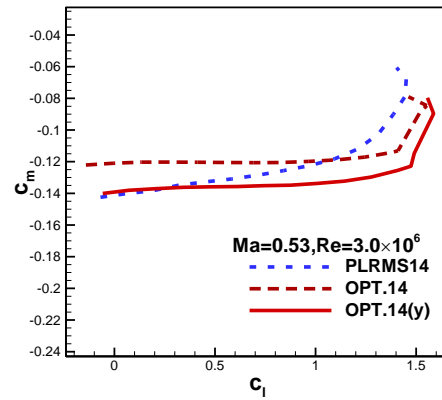


Figure 37. Comparison of the moment coefficients among baseline and optimized airfoils with and without geometric compatibility (14%c)

B.2 Design of 16% thick airfoil with geometric compatibility constraints

The design conditions are the same as section A.3. The mathematical model for aerodynamic optimization is described as follows:

$$\begin{aligned}
 &\text{objective} && \min c_d \\
 &\text{s.t.} && 0.15 - |c_m| \geq 0 \\
 &&& \text{thk} - 0.16 \geq 0 \\
 &&& |x_{\max \text{thk}} - x_{\max \text{thk}, 14\%c}| \leq 0.01 \\
 &&& \min(y_{\text{upper}} - y_{\text{upper}, 14\%c}) \geq 0 \\
 &&& \min(y_{\text{lower}, 14\%c} - y_{\text{lower}}) \geq 0
 \end{aligned} \tag{6}$$

where, the subscript 14%c is the optimized airfoil with 14%c thick in section B.1.

The comparison of shapes and pressure distribution between baseline and optimized airfoil with and without geometric compatibility are shown in Figure 38 and Figure 39. The optimized airfoil of 16% thickness without geometric compatibility constraints is partially inside the airfoil of 14% thickness, especially near the trailing edge on upper surface. While the optimized airfoil of 16% thickness with geometric compatibility constraints can fully surround the airfoil of 14% thickness.

The aerodynamic force coefficients of baseline and optimized airfoil with geometric compatibility at design condition are listed in Table 7. The drag coefficient is reduced by 15.7%, of which the friction drag accounts for 25.5%. Both the pressure drag and friction drag are reduced. Therefore, the lift-to-drag ratio has an increment by 18.6%. The performance curves of baseline and optimized airfoil are shown in Figure 40 to Figure 43. The optimized airfoil with geometric compatibility has a lower maximum lift coefficient, wide range of lower drag and lower lift-to-drag ratio than baseline airfoil.

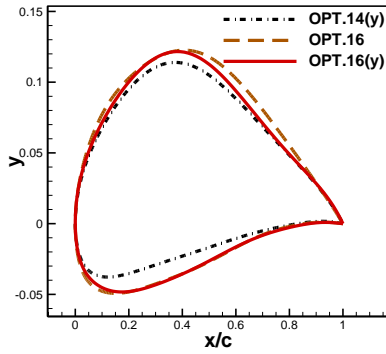


Figure 38. Comparison of the geometric shapes between adjacent and optimized airfoils with and without geometric compatibility (16% c)

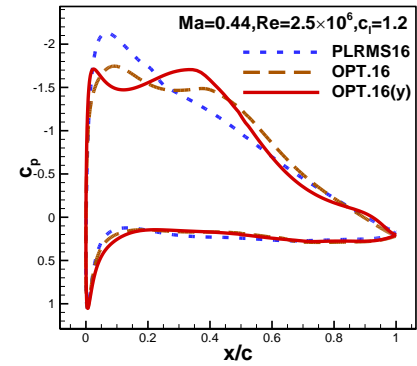
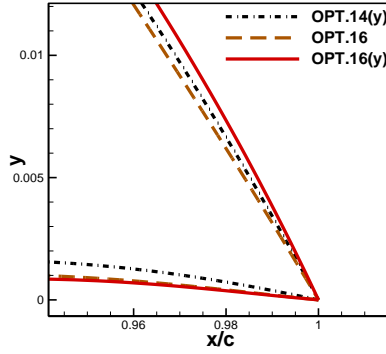


Figure 39. Comparison of the pressure distributions between baseline and optimized airfoils with and without geometric compatibility (16% c)

Table 7 Comparison of aerodynamic force coefficients between baseline and optimized airfoil
($Ma = 0.44, Re = 2.5 \times 10^6, c_l = 1.2$)

	c_l	c_d	c_{dp}	c_{df}	c_m	L/D
Baseline airfoil	1.2	0.011270	0.006624	0.004646	-0.111978	106.48
Optimized airfoil	1.2	0.009506	0.005309	0.004197	-0.124149	126.24
Δ	/	-0.001764	-0.00132	-0.000449	-0.012171	+19.76
$\Delta(\%)$	/	-15.65	-19.93	-9.66	/	+18.56

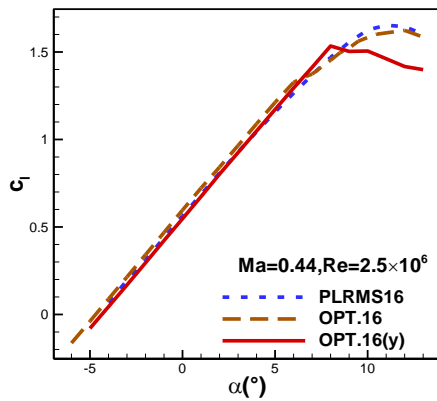


Figure 40. Comparison of the lift coefficients among baseline and optimized airfoils with and without geometric compatibility (16% c)

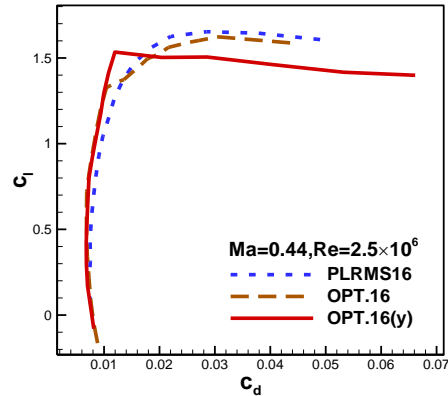


Figure 41. Comparison of the polar curves among baseline and optimized airfoils with and without geometric compatibility (16% c)

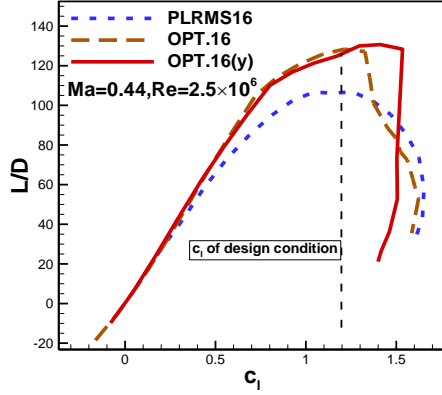


Figure 42. Comparison of the lift-drag ratio among baseline and optimized airfoils with and without geometric compatibility (16%c)

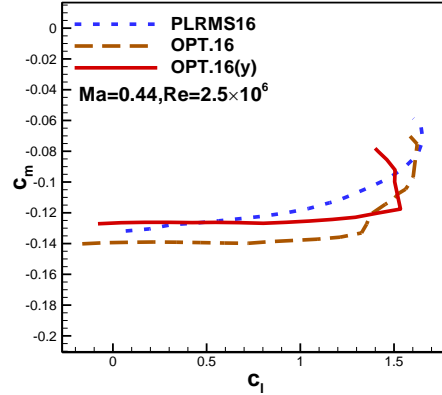


Figure 43. Comparison of the moment coefficients among baseline and optimized airfoils with and without geometric compatibility (16%c)

B.3 Design of 20% thick airfoil with geometric compatibility constraints

The design conditions are the same as section A.4. The mathematical model for aerodynamic optimization is described as follows:

$$\begin{aligned}
 &\text{objective} && \min c_d \\
 &\text{s.t.} && 0.15 - |c_m| \geq 0 \\
 &&& \text{thk} - 0.20 \geq 0 \\
 &&& |x_{\max \text{thk}} - x_{\max \text{thk}, 16\%c}| \leq 0.01 \\
 &&& \min(y_{\text{upper}} - y_{\text{upper}, 16\%c}) \geq 0 \\
 &&& \min(y_{\text{lower}, 16\%c} - y_{\text{lower}}) \geq 0
 \end{aligned} \tag{7}$$

where, the subscript 16%c is the optimized airfoil with 16%c thick in section B.2.

The comparison of shapes and pressure distribution are shown in Figure 44 and Figure 45. The optimized airfoil of 20% thickness without geometric compatibility constraints is partially inside the airfoil of 16% thickness, while the optimized airfoil with geometric compatibility constraints can fully surround the airfoil of 16% thickness. The pressure distributions of the optimized airfoils with and without geometric compatibility constraints are different. The optimized airfoil with geometric compatibility constraints has a gentle favorable pressure gradient and a lower peak of pressure, which helps to maintain laminar flow.

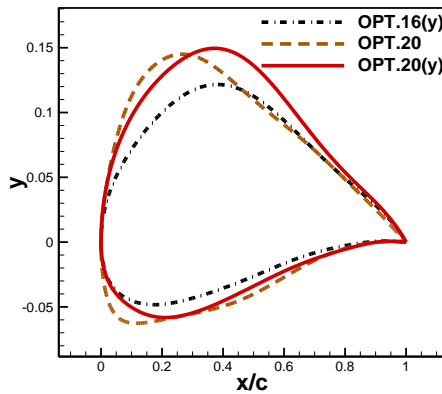


Figure 44. Comparison of the geometric shapes between adjacent and optimized airfoils with and without geometric compatibility (20%c)

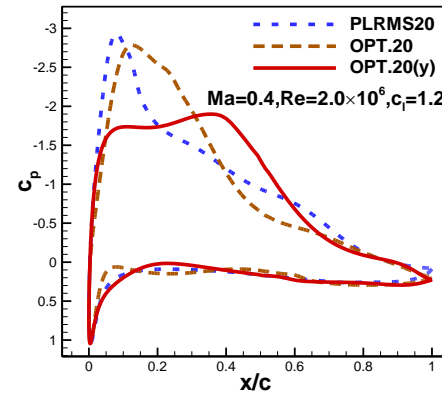


Figure 45. Comparison of the pressure distributions between baseline and optimized airfoils with and without geometric compatibility (20%c)

The aerodynamic force coefficients of baseline and optimized airfoil with geometric compatibility at the design condition are listed in Table 8. The drag coefficient is reduced by 37.2%, of which the pressure drag accounts for 87.6%. The friction drag is reduced by 14.59%. Therefore, the lift-to-drag ratio has a significant increment by 59.24%.

What shown in Figure 46 to Figure 49 is the comparison aerodynamic performance of baseline and the optimized airfoil with and without geometric compatibility. The maximum lift coefficient of the optimized airfoil is higher than that of the baseline airfoil, with a lower stall angle of attack. The drag coefficients of the optimized airfoil under almost all lift coefficients are reduced while the drag of the optimized airfoil with geometric compatibility is lower in a wide range of lift coefficients. Thus, the lift-to-drag ratio is significantly improved.

Table 8 Comparison of aerodynamic force coefficients between baseline and optimized airfoils

($Ma = 0.40, Re = 2.0 \times 10^6, c_l = 1.2$)

	c_l	c_d	c_{dp}	c_{df}	c_m	L/D
Baseline airfoil	1.2	0.016758	0.01142633	0.00533167	-0.095691	71.61
Optimized airfoil	1.2	0.010524	0.00597	0.004554	-0.123473	114.03
Δ	/	-0.006234	-0.00546	-0.00078	-0.02778	+42.4175
$\Delta(\%)$	/	-37.20	-47.75	-14.59	/	+59.24

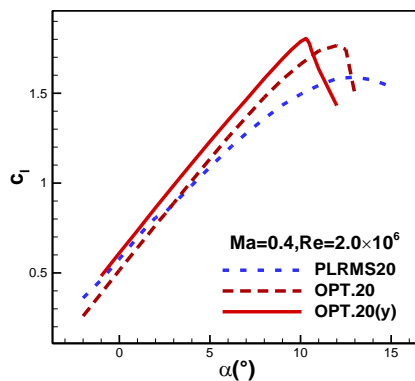


Figure 46. Comparison of the lift coefficients among baseline and optimized airfoils with and without geometric compatibility (20%c)

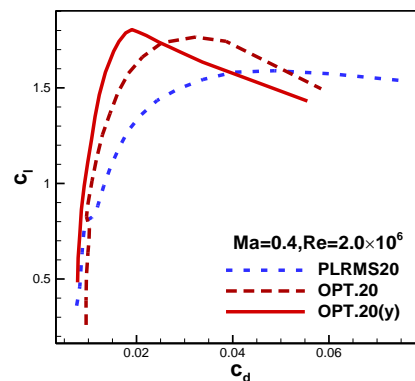


Figure 47. Comparison of the polar curves among baseline and optimized airfoils with and without geometric compatibility (20%c)

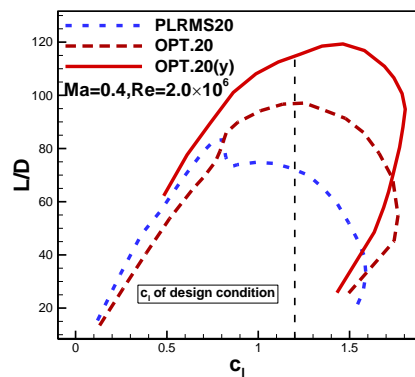


Figure 48. Comparison of the lift-drag ratio among baseline and optimized airfoils with and without geometric compatibility (20%c)

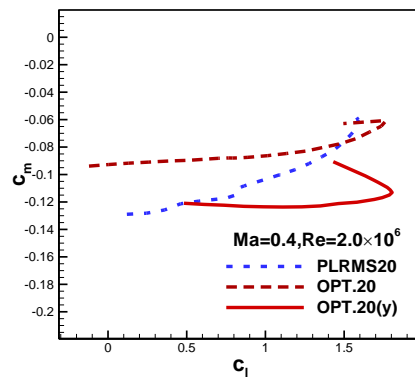


Figure 49. Comparison of the moment coefficients among baseline and optimized airfoils with and without geometric compatibility (20%c)

C. Geometric Compatibility Constraints: Second-order derivative distribution of the airfoil geometry

Although the location of maximum thickness and coordinates of airfoils with adjacent thickness can significantly improve the geometric compatibility, the second-order derivative distributions of the optimized airfoils in section B are checked in Figure 50, which shows poor compatibility. Therefore, in this section, second-order derivative constraint is added to optimization model, shown in formulas (8), (9), (10). The airfoils with 14%c, 16%c and 20%c thickness are optimized.

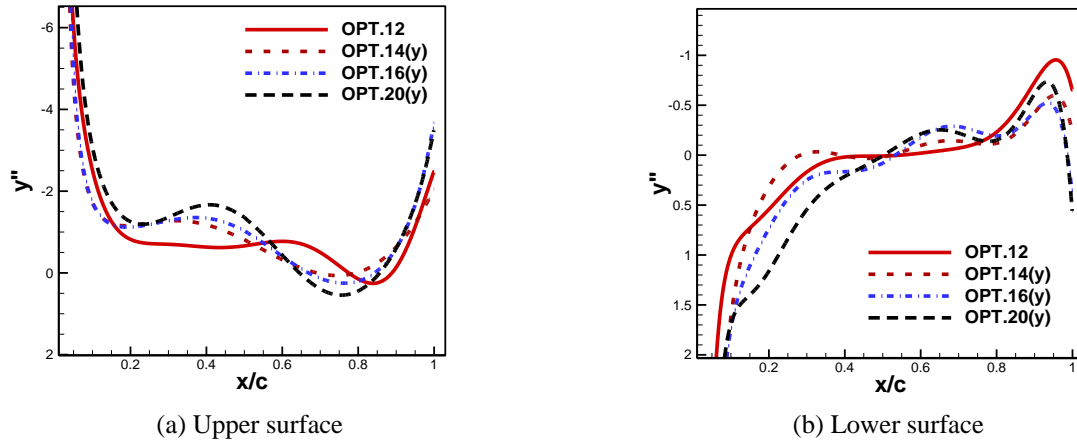


Figure 50. Second-order derivative distributions of the optimized airfoil in section B

C.1 Design of 14% thick airfoil with second-order derivative distributions constraints

The design conditions are the same as section A.2. The mathematical model for aerodynamic optimization of 14% thick airfoil in this section is described as follows:

$$\begin{aligned}
 &\text{objective} && \min c_d \\
 &\text{s.t.} && 0.15 - |c_m| \geq 0 \\
 &&& \text{thk} - 0.14 \geq 0 \\
 &&& \min(y''_{\text{upper},12\%c} - y''_{\text{upper}}) \geq 0 \\
 &&& \min(y''_{\text{lower}} - y''_{\text{lower},12\%c}) \geq 0
 \end{aligned} \tag{8}$$

where, the subscript “12%c” is the optimized airfoil with 12%c thick in section A.1.

The comparison of shapes and pressure distribution are shown in Figure 51 and Figure 52, and the second-order derivative distribution of adjacent and the optimized airfoil are presented in Figure 53. The geometry of both the optimized airfoils can fully surround the airfoil of 12%c thickness, while the optimized airfoil with second-order derivative constraints is more compatible with the adjacent airfoil of 12%c thickness. Different from Figure 50, the optimized airfoil with second-order derivative constraints has more similar second-order derivate and is more compatible in geometry with adjacent airfoil of 12%c thickness.

The aerodynamic force coefficients of baseline and optimized airfoil at design condition are listed in Table 9. The drag coefficient is reduced by 15.44%, of which the friction drag accounts for 48%. Therefore, the lift-to-drag ratio has a significant increment by 18.26%.

Figure 54 to Figure 57 show the comparison of aerodynamic performance among baseline and optimized airfoils. The optimized airfoil with second-order derivate constraints has higher maximum lift coefficient than that of the baseline airfoil, with higher stall angle of attack. The drag coefficients under almost all lift coefficients are slightly reduced. Therefore, the lift-to-drag ratio is significantly improved, especially near the design lift coefficient.

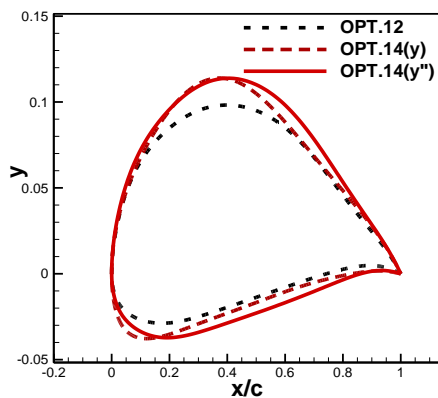


Figure 51. Comparison of the geometric shapes between adjacent and optimized airfoils with and without second-order derivative (14% c)

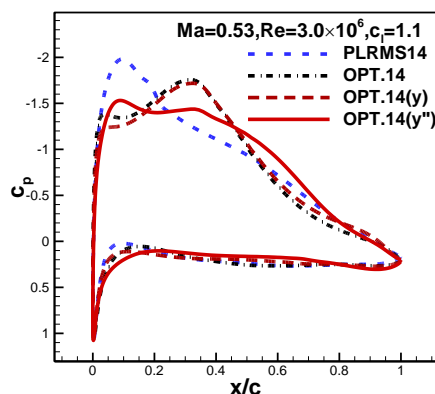
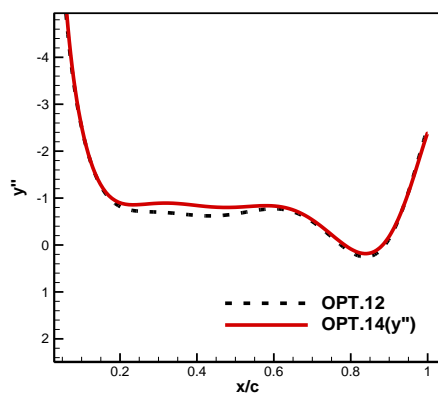
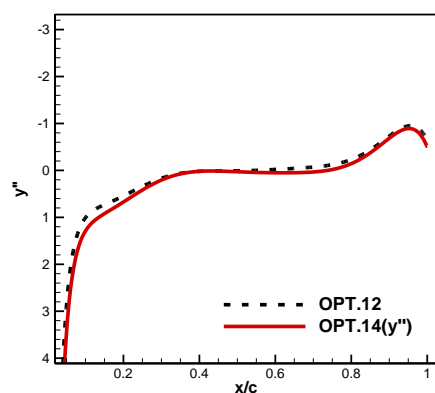


Figure 52. Comparison of the pressure distributions between baseline and optimized airfoils with and without geometric compatibility (14% c)



(a) Upper surface



(b) Lower surface

Figure 53. Comparison of the second-order derivative distributions between adjacent and optimized airfoils

Table 9 Comparison of aerodynamic force coefficients between baseline and optimized airfoils
($Ma = 0.53, Re = 3.0 \times 10^6, c_l = 1.1$)

	c_l	c_d	c_{dp}	c_{df}	c_m	L/D
Baseline airfoil	1.1	0.010620	0.005660	0.004960	-0.118156	103.58
Optimized airfoil	1.1	0.008980	0.004807	0.004173	-0.136976	122.49
Δ	/	-0.001640	-0.000853	-0.000787	-0.018820	+18.92
$\Delta(\%)$	/	-15.44	-15.07	-15.87	/	+18.26

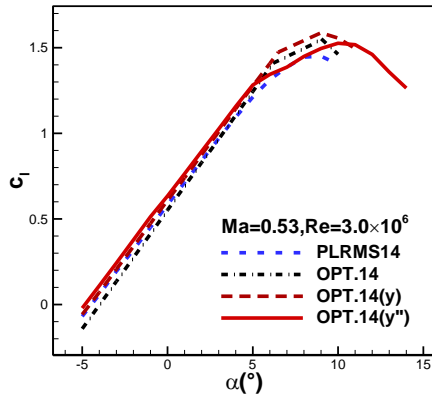


Figure 54. Comparison of the lift coefficients among baseline and optimized airfoils with and without geometric compatibility (14%c)

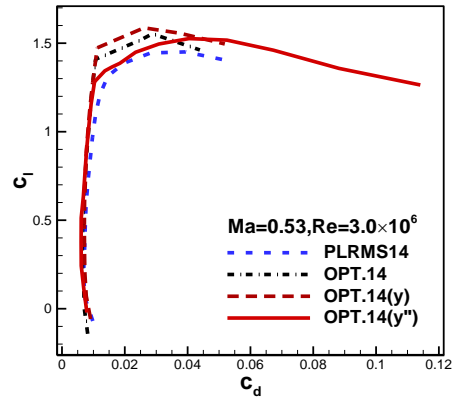


Figure 55. Comparison of the polar curves among baseline and optimized airfoils with and without geometric compatibility (14%c)

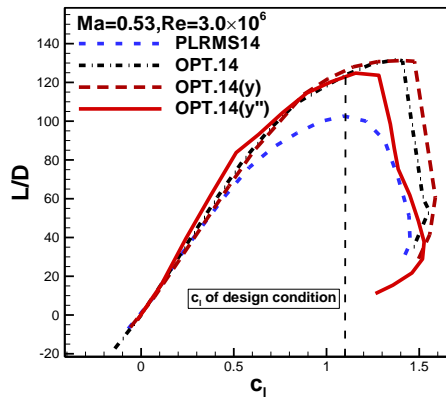


Figure 56. Comparison of the lift-drag ratio among baseline and optimized airfoils with and without geometric compatibility (14%c)

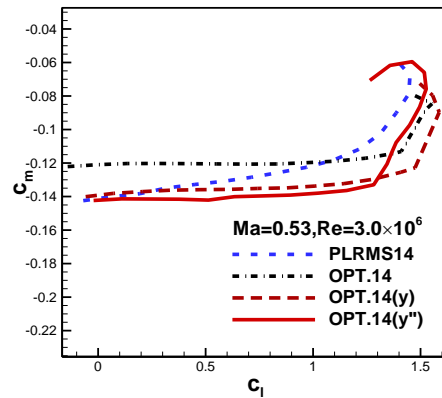


Figure 57. Comparison of the moment coefficients among baseline and optimized airfoils with and without geometric compatibility (14%c)

C.2 Design of 16% thick airfoil with second-order derivative distributions constraints

The design conditions are the same as section A.3. The mathematical model for aerodynamic optimization of 16% thick airfoil in this section is described as follows:

$$\begin{aligned}
 &\text{objective} && \min c_d \\
 &\text{s.t.} && 0.15 - |c_m| \geq 0 \\
 &&& \text{thk} - 0.16 \geq 0 \\
 &&& \min(y''_{\text{upper},14\%c} - y''_{\text{upper}}) \geq 0 \\
 &&& \min(y''_{\text{lower}} - y''_{\text{lower},14\%c}) \geq 0
 \end{aligned} \tag{9}$$

where, the subscript "14%c" is the optimized airfoil with 14%c thick in section C.1.

The comparison of shapes and pressure distribution are shown in Figure 58 and Figure 59. The optimized airfoil has great geometry similarity with adjacent airfoil. Both of the optimized airfoils with and without second-order derivative constraints have reasonable pressure distributions.

The second-order derivative distribution of adjacent and optimized airfoil are presented in Figure 60. The optimized airfoil in this section has more similar second-order derivative distribution with adjacent airfoil compared to Figure 50, resulting a better geometric compatibility.

The aerodynamic force coefficients of baseline and optimized airfoil at design condition are listed in Table 10. The drag coefficient is reduced by 6.92%, of which the friction drag accounts for 84.1%. Therefore, the lift-to-drag ratio has an increment by 7.44%.

As shown in Figure 61 to Figure 64, the maximum lift coefficient of the optimized airfoil with second-order derivate constraints is reduced, but the stall angle of attack increases, and the drag coefficients are reduced slightly under 0.2-1.3 range of lift coefficients. Therefore, the lift-to-drag ratio is improved a bit over this range of lift coefficients. After stall, the lift-to-drag ratio falls dramatically.

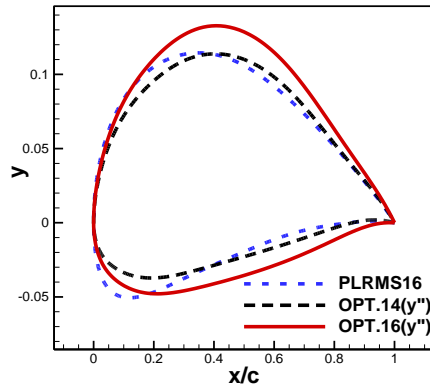


Figure 58. Comparison of the geometric shapes between baseline, adjacent and optimized airfoils with second-order derivative constraints (16% c)

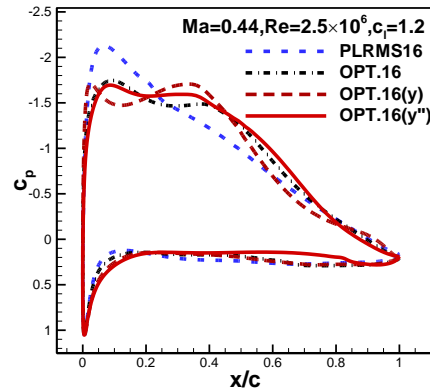
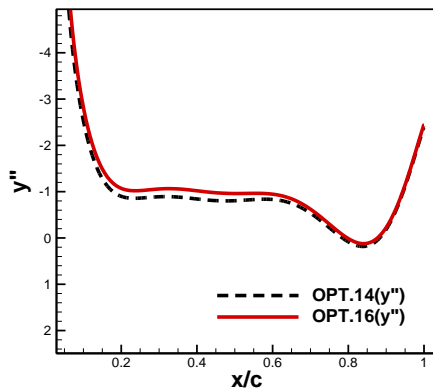
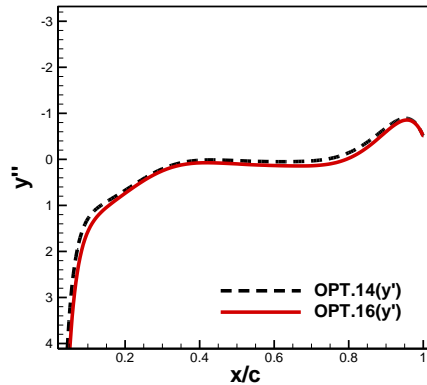


Figure 59. Comparison of the pressure distributions between baseline and optimized airfoils with and without geometric compatibility (16% c)



(a) Upper surface



(b) Lower surface

Figure 60. Comparison of the second-order derivative distributions between adjacent and optimized airfoils

Table 10 Comparison of aerodynamic force coefficients between baseline and optimized airfoils
($Ma = 0.44, Re = 2.5 \times 10^6, c_l = 1.2$)

	c_l	c_d	c_{dp}	c_{df}	c_m	L/D
Baseline airfoil	1.2	0.01127	0.006624	0.004646	-0.111978	106.48
Optimized airfoil	1.2	0.010490	0.006500	0.003990	-0.125533	114.39
Δ	/	-0.000780	-0.000124	-0.000656	-0.013555	+7.92
$\Delta(\%)$	/	-6.92	-1.87	-14.12	/	+7.44

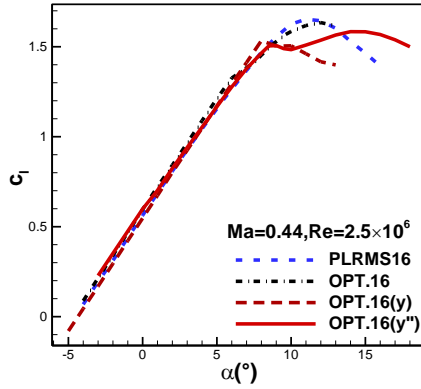


Figure 61. Comparison of the lift coefficients among baseline and optimized airfoils with and without geometric compatibility (16%c)

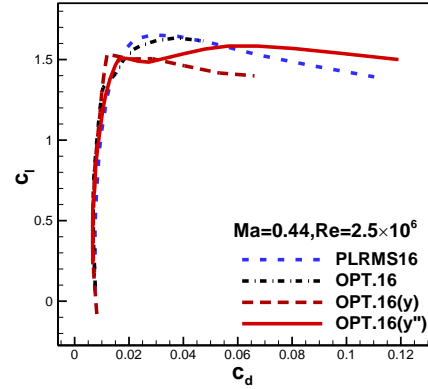


Figure 62. Comparison of the polar curves among baseline and optimized airfoils with and without geometric compatibility (16%c)

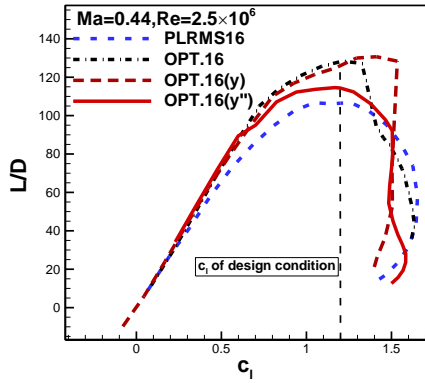


Figure 63. Comparison of the lift-drag ratio among baseline and optimized airfoils with and without geometric compatibility (16%c)

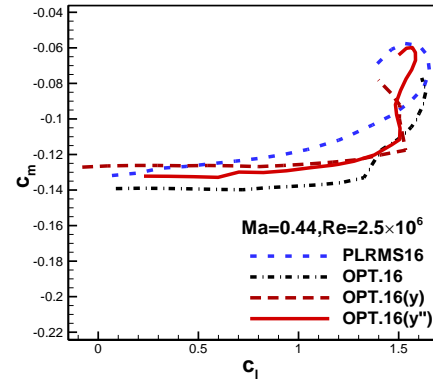


Figure 64. Comparison of the moment coefficients among baseline and optimized airfoils with and without geometric compatibility (16%c)

C.3 Design of 20% thick airfoil with second-order derivative distributions constraints

The design conditions are the same as section A.4. The mathematical model for aerodynamic optimization of 20% thick airfoil in this section is described as follows:

$$\begin{aligned}
 &\text{objective} && \min c_d \\
 &\text{s.t.} && 0.15 - |c_m| \geq 0 \\
 &&& \text{thk} - 0.20 \geq 0 \\
 &&& \min(y''_{\text{upper},16\%c} - y''_{\text{upper}}) \geq 0 \\
 &&& \min(y''_{\text{lower}} - y''_{\text{lower},16\%c}) \geq 0
 \end{aligned} \tag{10}$$

where, the subscript "16%c" is the optimized airfoil with 16%c thick in section C.2.

The comparison of shapes and pressure distributions are shown in Figure 65 and Figure 66. The optimized airfoil of 20%c thickness with second-order derivative constraints can fully surround the adjacent airfoil with 16%c thickness as well as the optimized airfoil without second-order derivative constraints. But the airfoil with second-order derivative constraints is more compatible with its adjacent airfoil. The second-order derivative distribution of adjacent and optimized airfoil are presented in Figure 67. The optimized airfoil in this section is more similar with second-order derivative distribution to adjacent airfoil, compared to Figure 50, resulting a better geometric compatibility.

The aerodynamic force coefficients of baseline and optimized airfoil at design condition are listed in Table 11. The total drag coefficient is reduced by 28.37%, of which the friction drag accounts for 28.7%. Thus, the lift-to-drag ratio increase by 39.6%. The aerodynamic performance comparison of baseline and optimized airfoils are shown in Figure 68 to Figure 71. The drag coefficients under a wide range of lift coefficients are reduced, so that the lift-to-drag ratio is improved in a wide range.

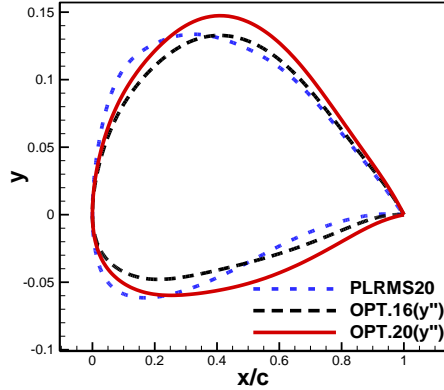


Figure 65. Comparison of the geometric shapes between baseline, adjacent and optimized airfoils with and without second-order derivative constraints (20% c)

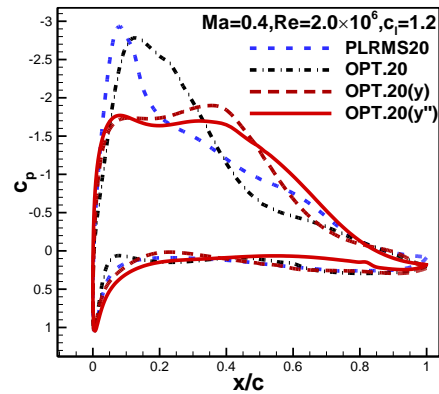
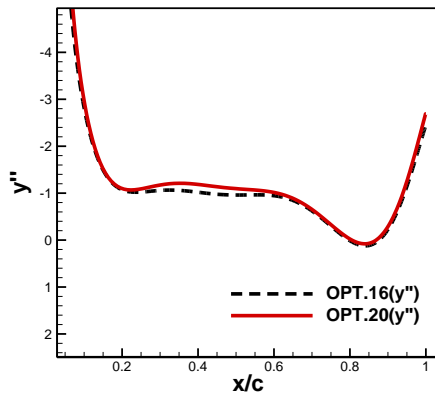
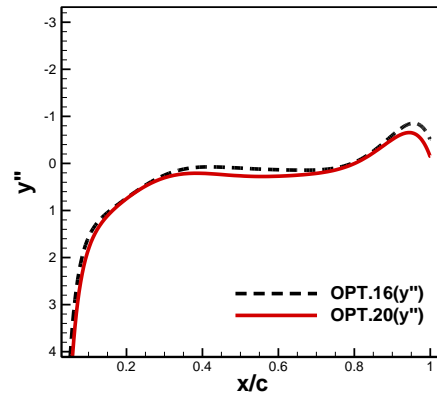


Figure 66. Comparison of the pressure distributions between baseline and optimized airfoils with and without geometric compatibility (20% c)



(a) Upper surface



(b) Lower surface

Figure 67. Comparison of the second-order derivative distributions between adjacent and optimized airfoils

Table 11 Comparison of aerodynamic force coefficients between baseline and optimized airfoils
($Ma = 0.40, Re = 2.0 \times 10^6, c_l = 1.2$)

	c_l	c_d	c_{dp}	c_{df}	c_m	L/D
Baseline airfoil	1.2	0.016758	0.011426	0.00533167	-0.095691	71.61
Optimized airfoil	1.2	0.012004	0.008036	0.003968	-0.109857	99.97
Δ	/	-0.004754	-0.003390	-0.001364	-0.014166	+28.36
$\Delta(\%)$	/	-28.37	-29.67	-25.58	/	+39.60

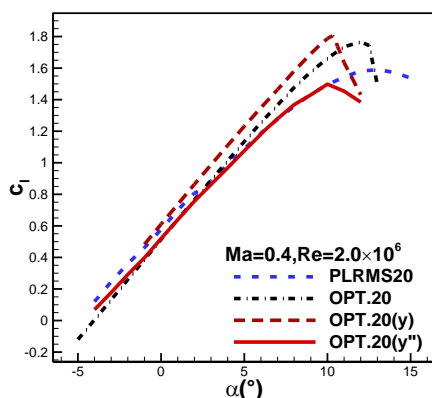


Figure 68. Comparison of the lift coefficients among baseline and optimized airfoils with and without geometric compatibility (20%c)

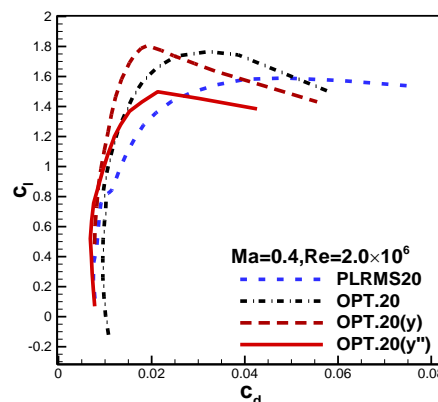


Figure 69. Comparison of the polar curves among baseline and optimized airfoils with and without geometric compatibility (20%c)

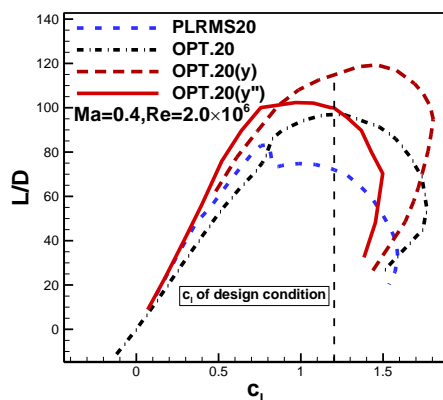


Figure 70. Comparison of the lift-drag ratio among baseline and optimized airfoils with and without geometric compatibility (20%c)

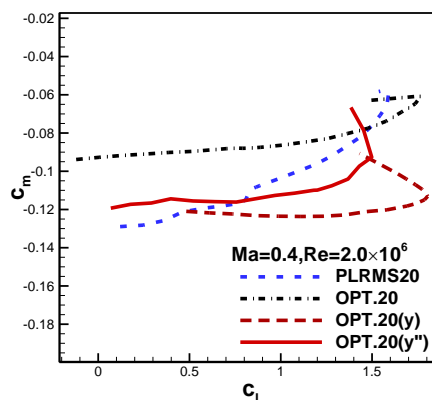


Figure 71. Comparison of the moment coefficients among baseline and optimized airfoils with and without geometric compatibility (20%c)

D. Comparison and Discussion

In this paper, 3 different types of constraints are proposed in the design optimization of a propeller airfoil family with 4 different thickness airfoils. The geometric shapes of the optimized airfoils with different constraints are presented in Figure 72, respectively. Obviously, the airfoil family with second-order derivate constraints has better geometric compatibility than those with other constraints. The second-order derivate curves of airfoils in this airfoil family appreciate similarity with each other like NACA series, as shown in Figure 73.

Due to the imposed stronger constraints, the lift-to-drag ratio of the optimized airfoils with second-order derivate constraints at design conditions is a little lower than those with other constraints, as shown in Figure 74. It demonstrates that the design of propeller airfoil family with geometric compatibility is a compromise between aerodynamic performance and geometric compatibility.

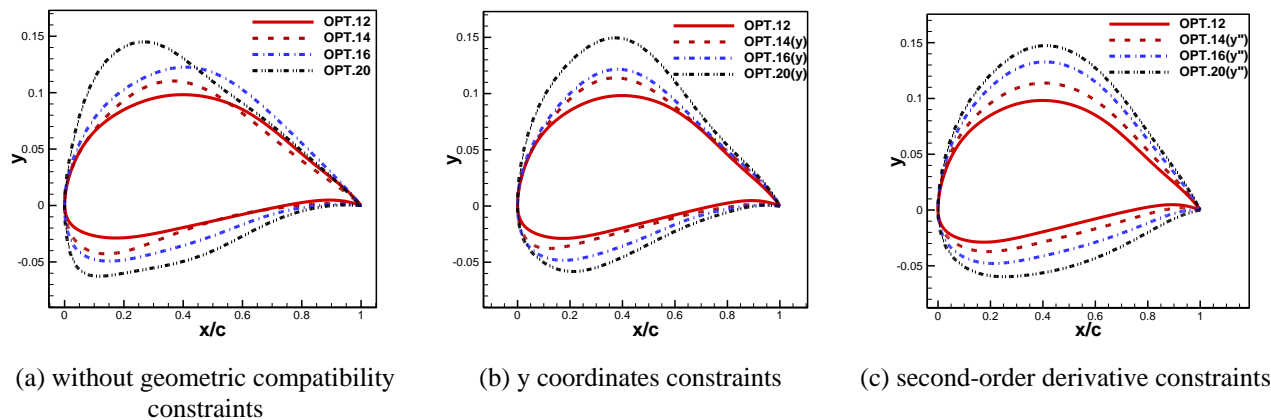


Figure 72. geometric shapes of the optimized airfoils in section A,B and C

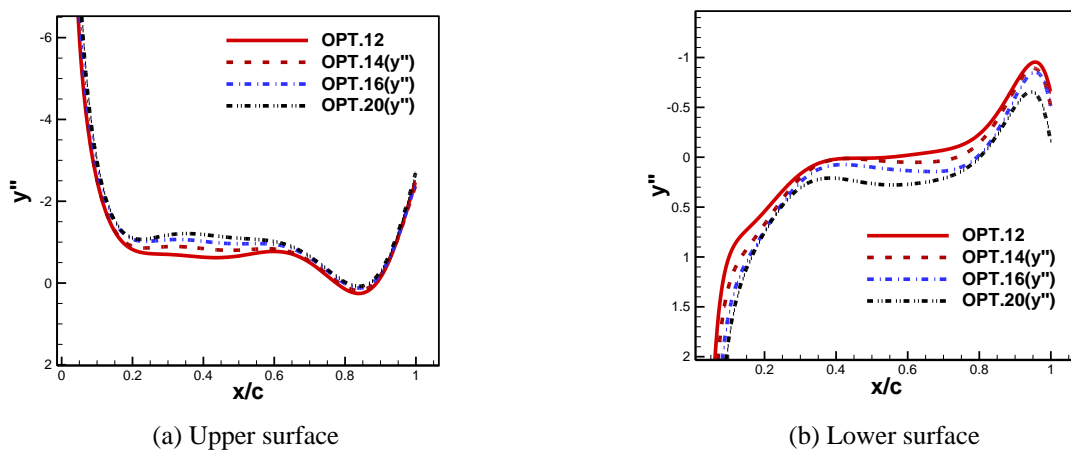


Figure 73. Second-order derivative distributions of the optimized airfoil in section C

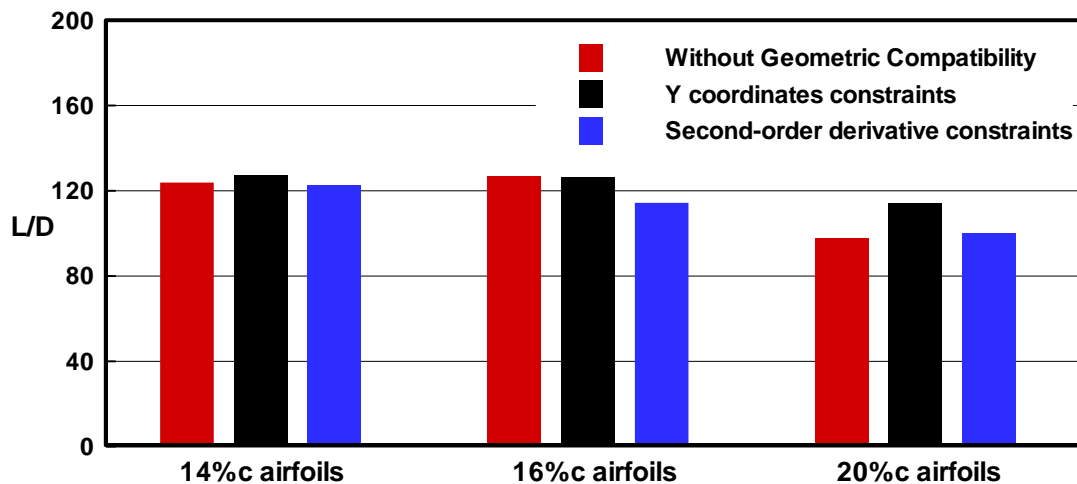


Figure 74. Lift-to-drag ratio of optimized airfoils at design conditions with different constraints

IV. Concluding Remarks

A new method for propeller airfoil family design is proposed, which can not only improve the aerodynamic performance of single airfoil, but also consider the geometric compatibility of airfoils with different thickness. To consider geometric compatibility, constraints including the locations of maximum thickness and coordinates of airfoils with adjacent thickness, and second-order derivative distribution of airfoil shape, are applied in the process of design optimization. Although the aerodynamic performance of airfoils with second-order derivative constraints is a little lower than airfoils with other constraints, the geometric compatibility is the best, which demonstrates that the second-order derivative constraints proposed in this paper can significantly improve geometric compatibility of propeller airfoils.

References

- [1] PeiQing. Liu., Theory and Application of Air Propeller, 2006.
- [2] Harold Y. Multi-point Design and Optimization of a Natural Laminar Flow Airfoil for a Mission Adaptive Compliant Wing[R].AIAA Paper 2008-293.
- [3] Jender L, Antony J. Natural-laminar-flow Airfoil and Wing Design by Adjoint Method and Automatic Transition Prediction[R]. AIAA Paper 2009-897,2009.
- [4] Taverna F . Advanced airfoil design for general aviation propellers[J]. Journal of Aircraft, 1984, 21(9):649-657.
- [5] K. R. Srilatha,G. S. Dwarakanath,P. Ramamoorthy. Design of a Natural Laminar Flow Airfoil for the Light Transport Aircraft[J]. Acta Mechanica,1990,85(3-4).
- [6] Green B E. An Approach to the Constrained Design of Natural Laminar Flow Airfoils[M]. NASA Langley Technical Report Server, 1997.
- [7] Jeffrey K. Jepson, Ashok Gopalarathnam. Incorporation of Aircraft Performance Considerations in Inverse Airfoil Design[J]. Journal of aircraft, 2005, 42(1).
- [8] Shen X , Avital E , Rezaienia M , et al. Computational methods for investigation of surface curvature effects on airfoil boundary layer behavior[J]. Journal of Algorithms & Computational Technology, 2016.
- [9] D. Greenblatt, I. Wygnanski , Effect of Leading-Edge Curvature on Airfoil Separation Control[J]. Journal of Aircraft, 2003, 40(3).
- [10] Z. H. Han. Efficient Method for Simulation of Viscous Flows past Helicopter Rotors and Active Flow Control. D. Dissertation, Northwestern Polytechnical Univ.,2007.
- [11] Menter F R, Langtry R B, Likki S R, et al. A Correlation-Based Transition Model Using Local Variables—Part I: Model Formulation[J]. Journal of Turbomachinery, 2006, 128(3).
- [12] S. Nadarajah McGill University Montreal, Canada. Aerodynamic Design Optimization:Drag Minimization of the RAE 2822 in Transonic Viscous Flow.
- [13] DM Somers. Design and Experimental Results for the S809 Airfoil.[R] NREL/SR-440-6918.
- [14] Krige, D. G. "A Statistical Approach to Some Basic Mine Valuation Problems on the Witwatersrand." *OR* 4.1(1953):18-18.
- [15] Jones, Donald R., M. Schonlau, and W. J. Welch. Efficient Global Optimization of Expensive Black-Box Functions. Kluwer Academic Publishers, 1998.
- [16] Han, Z.-H., SurroOpt: a Generic Surrogate-Based Optimization Code for Aerodynamic and Multidisciplinary Design[C]// 30th Congress of the International Council of the Aeronautical Sciences, 2016.
- [17] Kulfan, Brenda, and J. Bussoletti. "'Fundamental" Parametric Geometry Representations for Aircraft Component Shapes." AIAA Paper 2006:1--45.
- [18] Kulfan B M. A Universal Parametric Geometry Representation Method——“CST”. AIAA-2007-0062.